Comparison of Natural Convection Around a Circular Cylinder With Different Geometries of Cylinders Inside a Square Enclosure Filled With Ag-Nanofluid Superposed Porous-Nanofluid Layers

Salam Hadi Hussain[1]
Department of Automobile Engineering,
College of Engineering-Al Musayab,
Babylon University,
Babylon Province 00964-7802431066, Iraq
e-mails: salamphd1974@yahoo.com;
met.salam.hadi@uobabylon.edu.iq

Mustafa Salah Rahomey
Mechanical Engineering Department,
College of Engineering,
Babylon University,
Babylon Province 00964-7802431066, Iraq

Numerical simulations are carried out for fluid flow and natural convection heat transfer induced by a temperature difference between a hot inner cylinder with different geometries (i.e., circular; triangular; elliptic; rectangular; and rhombic) and a cold outer square enclosure filled with nanofluid superposed porous-nanofluid layers. The Darcy–Brinkman model is applied for the saturated porous layer with nanofluid. Moreover, the transport equations (mass, momentum, and energy) are solved numerically using the Galerkin weighted residual method by dividing the domain into two sets of equations for every layer with incorporating a nonuniform mesh size. The considered domains in this investigation are closely examined over a wide range of Rayleigh number ($10^3 \leq Ra \leq 10^6$), Darcy number ($10^{-5} \leq Da \leq 10^{-1}$), the thickness of porous layer ($0\% \leq X_p \leq 100\%$), thermal conductivity ratio ($1 \leq R_k \leq 20$), and nanoparticle volume fraction ($0 \leq \varphi \leq 0.1$), respectively. The nanofluid is considered to be composed of Ag-nanoparticle and water as a base fluid. The results showed that the obtained total surfaces-averaged Nusselt numbers of the enclosure, in all cases, at the same operating conditions, the rate of heat transfer from the outer enclosure which the triangular cylinder is located inside is better. Also, as the thickness of the porous layer is increased from 20% to 80%, the free convection performance will decrease significantly (to about 50%) due to the hydrodynamic properties of the porous material. [DOI: 10.1115/1.4039642]

Keywords: natural convection, square enclosure, circular cylinder, different geometries, Ag-nanofluid, two layers, Darcy–Brinkman model, finite element method

1 Introduction

Interest of natural convection heat transfer and fluid flow in a confined cavity partly filled with a fluid layer and partly with a porous layer saturated by the same fluid have been motivated by a broad range of industrial and environmental applications, including geothermal systems, fuel cell, crude oil production, storage of nuclear waste materials, solar collectors, ground water pollution, fiber and granular insulations, solidification, etc. A multilayer flow plays an important role in a wide variety of fluid systems in nature. For example, in the nuclear plants, the porous material works on damping (or slow) the fluid flow, in order to allow time of heat exchange, and thus increases the efficiency and capacity of the cooling or heat transfer. Because of this wide range of applications, so far, many experimental and numerical studies have been performed in this field including different geometric forms. For example, Kahwaji and Ali [1] investigated numerically the enhancement of natural convection heat transfer with square internal cylinder using nanofluids. It used water-based Cu as the working nanofluid. They used a range of ($10^4 \leq Ra \leq 10^6$), ($0 \leq \varphi \leq 0.2$), enclosure width to cylinder height ratio (W/H) of 2.5. The results showed that an increase in average Nusselt number with increasing the volume fraction of the nanoparticles for the whole range of Rayleigh numbers. Munshi et al. [2] used the Magneto-hydrodynamic (MHD) field on buoyancy-driven free convection heat transfer in a square enclosure with the inner square shape heated block kept the centre. The horizontal bottom wall of the enclosure is nonuniformly heated. While the side walls of the cavity were maintained at a cold temperature, and the upper wall is adiabatic. While the natural convection around a tilted heated square cylinder in an enclosure in the range of ($10^3 \leq Ra \leq 10^6$) was studied by De and Dalal [3], Chamkha et al. [4] performed the study of two-dimensional (2D) mixed convection from a heated square solid cylinder located at the center of a vented cavity filled with air ($Pr = 0.71$). It is also possible to note that the results did not change much when using the rectangular cylinder compared with the square cylinder, and this is what was observed in the researchers [5,6]. As for the researchers who studied a triangular cylinder, El Abdallaoui et al. [7] studied numerically of natural convection around a decentered triangular cylinder placed in a square cylinder using the Lattice–Boltzmann method. They used the range of data, ($10^3 \leq Ra \leq 10^7$), ($Pr = 7$), and ($0 < \varphi < 0.1$). The results obtained show that the fluid flow and heat transfer characteristics were highly affected by the heating cylinder position. The authors in Refs. [8–10] used the horizontal cylindrical annuli with inner triangular cylinder.

The fundamental features of natural convection inside enclosures within the circular cylinder have been identified and

[1]Corresponding author.

Contributed by the Heat Transfer Division of ASME for publication in the Journal of Heat Transfer. Manuscript received July 14, 2017; final manuscript received March 1, 2018; published online November 26, 2018. Assoc. Editor: Antonio Barletta.

analyzed, in several studies in literature. Some studies were focusing on studying the changing position of the circular cylinder vertically and representative investigations on this topic and can be found in Refs. [11–13], and another group studied the change of location diagonally [14], while specialty rest group were studied the effect of changing the diameter of the internal cylinder such as Seo et al. [15], on other hand, some literatures concerned with the rotation of internal cylinder inside an enclosure as reported in Refs. [16] and [17]. Chamkha et al. [18] investigated numerically the mixed convection in a square cavity that has a fluid and superposed porous medium with an adiabatic rotating circular cylinder. They found that the averaged heat transfer increases almost linearly with the angular rotational velocity of the cylinder and the increase rate becomes higher as the cylinder size increases. Aly et al. [19] reported a numerical investigation of an unsteady mixed convection in a lid-driven square cavity that included circular cylinder motion using an incompressible smoothed particle hydrodynamic method. They predicted that significant heat transfer enhancement could be obtained due to the presence of moving circular cylinders inside the fluid flows. While Gibanov et al. [20] investigated numerically a mixed convection in a square cavity having a triangular porous layer and a local heater, the finite difference method is used to solve the governing partial differential equations with corresponding boundary conditions by using the dimensionless stream function, vorticity, and temperature formulation. Khozeymehnezhad and Mirbozorgi [21] carried out a comparison of natural convection around a circular cylinder with a square cylinder inside a square enclosure at the range of Rayleigh number (10^3–10^5). They obtained that in all cases, at the same Rayleigh number, the rate of heat transfer from the enclosure, in which the circular cylinder is located inside, is better than the square cylinder. Parmananda et al. [22] studied critical assessment of numerical algorithms for convective-radiative heat transfer in enclosures with different geometries. They showed that the entropy generation analysis in square geometry is the optimum design among the three geometries of heated cylinder as it has the maximum heat transfer and minimum entropy generation. On other hand, Bararnia et al. [23] studied numerically the natural convection between a square outer cylinder and a heated elliptic inner cylinder. The authors used Lattice Boltzmann method to investigate the hydrodynamic and thermal behaviors of the fluid at various vertical positions of the inner cylinder for different Rayleigh numbers ranging from 10^3 to 10^6. Also, Kalyana Raman et al. [24] and Zhang et al. [25] performed a detailed study about the free convection over a heated elliptic cylinder. They found that the surface-averaged Nusselt number increases with increasing the Rayleigh number. Roslan et al. [26] presented a numerical study to analyze the conjugate natural convection heat transfer in a differentially heated square enclosure containing a conductive polygon object. The governing equations were solved numerically by the COMSOL MULTIPHYSICS software. The governing parameters considered are the polygon type, ($3 \leq N \leq \infty$), the horizontal position, ($0.25 \leq X \leq 0.75$), the polygon size, ($0 \leq A \leq \pi/16$), the thermal conductivity ratio, ($0.1 \leq K_r \leq 10.0$), and the Rayleigh number, ($10^3 \leq \mathrm{Ra} \leq 10^6$). Tayebi et al. [27] investigated numerically the natural convection fluid flow and heat transfer in an annulus of two differentially heated confocal elliptic cylinders filled with the Cu–water nanofluid. The results obtained that the heat transfer enhances with increasing the Rayleigh number, but its effect is more pronounced for largest gap between the cylinders. Said et al. [28] dedicated the numerical simulation of thermal convection in a two-dimensional vertical conical cylinder partially annular space. They obtained that the results in terms of Nusselt number had been found between the present previsions and available data from the published literature data. Chamkha and Ismael [29,30] studied the conjugate natural convection-conduction heat transfer in a square domain composed of a cavity heated by a triangular solid wall under steady-state condition. Sheremet and Trifonova [31] studied numerically a transient natural convection in a vertical cylinder containing both a fluid layer overlying a horizontal porous layer saturated with the same fluid and heat-conducting solid shell of finite thickness in conditions of convective heat exchange with an environment. The authors considered the Beavers–Joseph empirical boundary condition at the fluid porous interface with the Darcy model for the porous layer and the Boussinesq approximation for the pure fluid. In another study [32], the other researchers studied the transient natural convection in a vertical cylinder partially filled with a porous media with heat-conducting solid walls of finite thickness in conditions of convective heat exchange with an environment. The main objective was to investigate the influence of Darcy number $10^{-5} \leq \mathrm{Da} \leq 10^{-3}$, porous layer height ratio $0 \leq d/L \leq 1$, thermal conductivity ratio $1 \leq k_{1,3} \leq 20$, and dimensionless time $0 \leq \tau \leq 1000$ on the fluid flow and heat transfer on the basis of the Darcy and non-Darcy models.

From the peered literature survey mentioned above and based upon our experience, there is no research or study up to date that conducted the natural convection heat transfer of a hot internal cylinder inside a cold square enclosure filled with two nanofluid-porous layers. Also, there is no comprehensive study that compares the natural convection around the internal cylinders with different geometries (i.e., circular, triangular, elliptic, rectangular and rhombic) inside a square enclosure. Therefore, in our opinion, this work gives an original scientific contribution in this significant field. In the present work, different features of the natural convection around the five different geometries of cylinders inside an enclosure filled with two nanofluid-porous layers are numerically investigated for different important parameters such as Rayleigh number ($10^3 \leq \mathrm{Ra} \leq 10^6$), Darcy number ($10^{-5} \leq \mathrm{Da} \leq 10^{-1}$), the thickness of porous layer ($0\% \leq X_p \leq 100\%$), thermal conductivity ratio ($1 \leq R_k \leq 20$), and nanoparticle volume fraction ($0 \leq \varphi \leq 0.1$).

2 Problem Description

The physical models used in the present work are shown in Fig. 1. A hot inner cylinder that has the same area compared with other type of cylinders is inserted into a square enclosure of

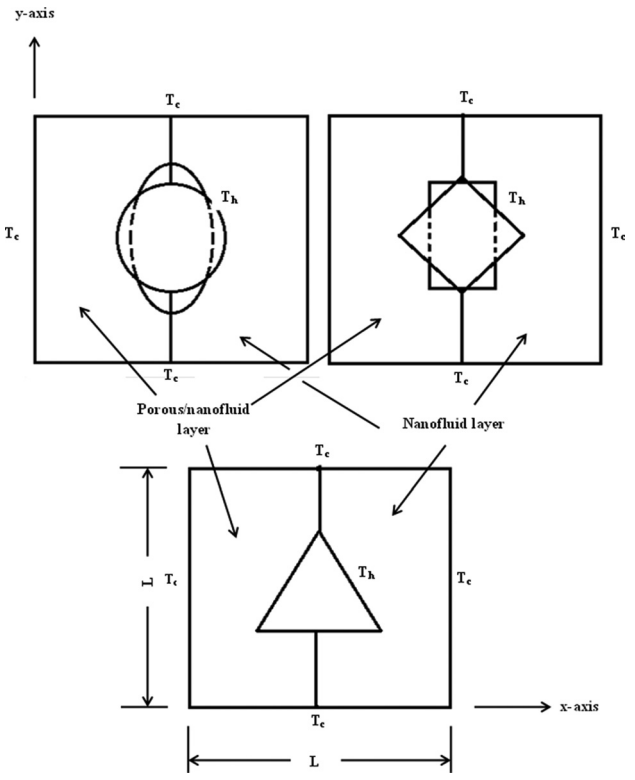

Fig. 1 Physical domains and coordinate system along with boundary conditions for five geometries

cooled walls with side length (L). The enclosure is divided by a permeable interface into two layers placed vertically. A vertical porous layer of thickness (X_p) is localized on the left part of cavity and saturated with a nanofluid. This nanofluid fills the remainder of the cavity ($L-X_p$). The outer surface of inner cylinder is heated isothermally and kept at (T_h), while the four side walls of outer square enclosure are cooled isothermally and kept at (T_c). The governing parameters, which are considered as an input data, are ($0\% \le X_p \le 100\%$, $10^3 \le \mathrm{Ra} \le 10^6$, $10^{-5} \le \mathrm{Da} \le 10^{-1}$, $1 \le R_k \le 20$ and $0 \le \varphi \le 0.1$), respectively.

2.1 Governing Equations for Two Layers System. The governing two-dimensional equations in the Cartesian coordinate system for the present study are described in this section by using the following assumptions; we consider the flow is steady, two-dimensional, incompressible, and laminar. Darcy–Brinkman model is considered for the flow prediction inside the porous media. The porous media has a homogenous and isotropic permeability. There are a local thermal equilibrium between the porous matrix and the fluid. Radiation mode of the heat transfer is considered negligible. Also, internal heat generation is neglected. The nanofluid thermophysical properties are assumed constant, except the density in the body force term in the momentum equation, which is treated according to the Boussinesq approximation which is

$$\rho = \rho_{\mathrm{nf}}[1 - \beta_{\mathrm{nf}}(T_h - T_c)] \tag{1}$$

Therefore, the continuity, momentum, and energy equations in the dimensional form for the present work are given by

A *For porous/nanofluid region, it is given by* [30]

$$\text{Continuity equation} \quad \frac{\partial u}{\partial x} + \frac{\partial v}{\partial y} = 0 \tag{2}$$

Momentum equation

$$x - \mathrm{dir}\left(u\frac{\partial u}{\partial x} + v\frac{\partial u}{\partial y}\right) = -\frac{1}{\rho_{\mathrm{nf}}}\frac{\partial p}{\partial x} + \frac{\mu_{\mathrm{nf}}}{\rho_{\mathrm{nf}}}\left(\frac{\partial^2 u}{\partial x^2} + \frac{\partial^2 u}{\partial y^2}\right) - \frac{\mu_{\mathrm{nf}}}{\rho_{\mathrm{nf}}K}u \tag{3}$$

$$y - \mathrm{dir}\left(u\frac{\partial v}{\partial x} + v\frac{\partial v}{\partial y}\right) = -\frac{1}{\rho_{\mathrm{nf}}}\frac{\partial p}{\partial y} + \frac{\mu_{\mathrm{nf}}}{\rho_{\mathrm{nf}}}\left(\frac{\partial^2 v}{\partial x^2} + \frac{\partial^2 v}{\partial y^2}\right) - \frac{\mu_{\mathrm{nf}}}{\rho_{\mathrm{nf}}K}v + \beta_{\mathrm{nf}}g(T_f - T_c) \tag{4}$$

$$\text{Energy equation } u\frac{\partial T}{\partial x} + v\frac{\partial T}{\partial y} = \alpha_{\mathrm{nf}}\left(\frac{\partial^2 T}{\partial x^2} + \frac{\partial^2 T}{\partial^2 y}\right) \tag{5}$$

B *For nanofluid region, it is given by* [30]

$$\text{Continuity equation} \frac{\partial u_{\mathrm{nf}}}{\partial x} + \frac{\partial v_{\mathrm{nf}}}{\partial y} = 0 \tag{6}$$

Momentum equation

$$x - \mathrm{dir}\left(u_{\mathrm{nf}}\frac{\partial u_{\mathrm{nf}}}{\partial x} + v_{\mathrm{nf}}\frac{\partial u_{\mathrm{nf}}}{\partial y}\right) = -\frac{1}{\rho_{\mathrm{nf}}}\frac{\partial p}{\partial x} + \frac{\mu_{\mathrm{nf}}}{\rho_{\mathrm{nf}}}\left(\frac{\partial^2 u_{\mathrm{nf}}}{\partial x^2} + \frac{\partial^2 u_{\mathrm{nf}}}{\partial y^2}\right) \tag{7}$$

$$y - \mathrm{dir}\left(u_{\mathrm{nf}}\frac{\partial v_{\mathrm{nf}}}{\partial x} + v_{\mathrm{nf}}\frac{\partial v_{\mathrm{nf}}}{\partial y}\right) = -\frac{1}{\rho_{\mathrm{nf}}}\frac{\partial p}{\partial y} + \frac{\mu_{\mathrm{nf}}}{\rho_{\mathrm{nf}}}\left(\frac{\partial^2 v_{\mathrm{nf}}}{\partial x^2} + \frac{\partial^2 v_{\mathrm{nf}}}{\partial y^2}\right) + \beta_{\mathrm{nf}}g(T_f - T_c) \tag{8}$$

$$\text{Energy equation } u_{\mathrm{nf}}\frac{\partial T}{\partial x} + v_{\mathrm{nf}}\frac{\partial T}{\partial y} = \alpha_{\mathrm{nf}}\left(\frac{\partial^2 T}{\partial x^2} + \frac{\partial^2 T}{\partial^2 y}\right) \tag{9}$$

The following dimensionless variables can be written as follows:

$$X = \frac{x}{L}, \quad Y = \frac{y}{L}, \quad U = \frac{uL}{\alpha_f}, \quad V = \frac{vL}{\alpha_f}, \quad P = \frac{pL^2}{\rho_{\mathrm{nf}}\alpha_f^2}, \quad \theta = \frac{T - T_c}{\Delta T}, \quad \mathrm{Ra} = \frac{g\beta_f L^3 \Delta T}{\nu_f \alpha_f}, \quad \mathrm{Pr} = \frac{\nu_f}{\alpha_f} \tag{10}$$

The effective properties of nanofluid density (ρ_{nf}), thermal expansion coefficient $(\beta)_{\mathrm{nf}}$, heat capacitance $(C_p)_{\mathrm{nf}}$, and thermal diffusivity (α_{nf}) of the nanofluid can be defined, respectively, as can be written as follows [30]:

$$\rho_{\mathrm{nf}} = (1-\varphi)\rho_f + \varphi\rho_p \tag{11}$$

$$(\rho\beta)_{\mathrm{nf}} = (1-\varphi)(\rho\beta)_f + \varphi(\rho\beta)_p \tag{12}$$

$$(\rho C_p)_{\mathrm{nf}} = (1-\varphi)(\rho C_p)_f + \varphi(\rho C_p)_p \tag{13}$$

$$\alpha_{\mathrm{nf}} = \frac{k_{\mathrm{nf}}}{(\rho C_P)_{\mathrm{nf}}} \tag{14}$$

The viscosity of the nanofluid is defined according to the Brinkman model and considered as a function of the solid volume fraction as given by [30].

$$\mu_{\mathrm{nf}} = \frac{\mu_f}{(1-\varphi)^{2.5}} \tag{15}$$

While the Maxwell correlation of the thermal conductivity of the nanofluid is considered in the present work as given by can be written as follows [30]:

$$k_{\mathrm{nf}} = k_f\frac{(k_p + 2k_f) - 2\varphi(k_f - k_p)}{(k_p + 2k_f) + \varphi(k_f - k_p)} \tag{16}$$

The above equations (i.e., Eqs. (2)–(9)) with these dimensionless variables and using the properties of nanofluid can be written in terms of the following dimensionless variables as follows [30].

For porous/nanofluid region

$$\frac{\partial U}{\partial X} + \frac{\partial V}{\partial Y} = 0 \tag{17}$$

$$U\frac{\partial U}{\partial X} + V\frac{\partial U}{\partial Y} = -\frac{\partial P}{\partial X} + \frac{\mathrm{Pr}}{(1-\phi)^{2.5}}\frac{\rho_f}{\rho_{\mathrm{nf}}}\left(\frac{\partial^2 U}{\partial X^2} + \frac{\partial^2 U}{\partial Y^2}\right) - \frac{\mathrm{Pr}}{(1-\phi)^{2.5}}\frac{\rho_f}{\rho_{\mathrm{nf}}}\frac{U}{\mathrm{Da}} \tag{18}$$

$$U\frac{\partial V}{\partial X} + V\frac{\partial V}{\partial Y} = -\frac{\partial P}{\partial Y} + \frac{\mathrm{Pr}}{(1-\phi)^{2.5}}\frac{\rho_f}{\rho_{\mathrm{nf}}}\left(\frac{\partial^2 V}{\partial X^2} + \frac{\partial^2 V}{\partial Y^2}\right) - \frac{\mathrm{Pr}}{(1-\phi)^{2.5}}\frac{\rho_f}{\rho_{\mathrm{nf}}}\frac{V}{\mathrm{Da}} + \frac{(\rho\beta)_{\mathrm{nf}}}{\rho_{\mathrm{nf}}\beta_f}\mathrm{Ra}\ \mathrm{Pr}\ \Theta \tag{19}$$

$$U\frac{\partial\theta}{\partial X}+V\frac{\partial\theta}{\partial Y}=\frac{\alpha_{\mathrm{nf}}}{\alpha_f}\left(\frac{\partial^2\theta}{\partial X^2}+\frac{\partial^2\theta}{\partial Y^2}\right) \tag{20}$$

For nanofluid region

$$\frac{\partial U_{\mathrm{nf}}}{\partial X}+\frac{\partial V_{\mathrm{nf}}}{\partial Y}=0 \tag{21}$$

$$U_{\mathrm{nf}}\frac{\partial U_{\mathrm{nf}}}{\partial X}+V\frac{\partial U_{\mathrm{nf}}}{\partial Y}=-\frac{\partial P}{\partial X}+\frac{\mathrm{Pr}}{(1-\phi)^{2.5}}\frac{\rho_f}{\rho_{\mathrm{nf}}}\left(\frac{\partial^2 U_{\mathrm{nf}}}{\partial X^2}+\frac{\partial^2 U_{\mathrm{nf}}}{\partial Y^2}\right) \tag{22}$$

$$V_{\mathrm{nf}}\frac{\partial V_{\mathrm{nf}}}{\partial X}+V\frac{\partial V_{\mathrm{nf}}}{\partial Y}=-\frac{\partial P}{\partial Y}+\frac{\mathrm{Pr}}{(1-\phi)^{2.5}}\frac{\rho_f}{\rho_{\mathrm{nf}}}\left(\frac{\partial^2 V_{\mathrm{nf}}}{\partial X^2}+\frac{\partial^2 V_{\mathrm{nf}}}{\partial Y^2}\right)+\frac{(\rho\beta)_{\mathrm{nf}}}{\rho_{\mathrm{nf}}\beta_f}\mathrm{Ra}\ \mathrm{Pr}\ \Theta \tag{23}$$

$$U_{\mathrm{nf}}\frac{\partial\Theta_{\mathrm{nf}}}{\partial X}+V_{\mathrm{nf}}\frac{\partial\Theta_{\mathrm{nf}}}{\partial Y}=\frac{\alpha_{\mathrm{nf}}}{\alpha_f}\left(\frac{\partial^2\Theta_{\mathrm{nf}}}{\partial X^2}+\frac{\partial^2\Theta_{\mathrm{nf}}}{\partial^2 Y}\right) \tag{24}$$

The flow field inside the wavy cavities can be represented by the stream function, which is defined and can be written as follows [30]:

$$U=\frac{\partial\psi}{\partial Y},\quad V=-\frac{\partial\psi}{\partial X}\quad U_{\mathrm{nf}}=\frac{\partial\psi_{\mathrm{nf}}}{\partial Y},\quad V_{\mathrm{nf}}=-\frac{\partial\psi_{\mathrm{nf}}}{\partial X} \tag{25}$$

This gives the following dimensionless equation:

$$\frac{\partial^2\psi}{\partial X^2}+\frac{\partial^2\psi}{\partial Y^2}=\frac{\partial U}{\partial Y}-\frac{\partial V}{\partial X} \tag{26}$$

$$\frac{\partial^2\psi_{\mathrm{nf}}}{\partial X^2}+\frac{\partial^2\psi_{\mathrm{nf}}}{\partial Y^2}=\frac{\partial U_{\mathrm{nf}}}{\partial Y}-\frac{\partial V_{\mathrm{nf}}}{\partial X} \tag{27}$$

3 Boundary Conditions

The center of circular cylinder is located at the center of enclosure ($X=0.5$, $Y=0.5$) and the radius of the cylinder ($R=0.2L$). The dimensionless boundary conditions for this case are given by

(1) The sidewalls of the enclosure are maintained at a constant cold temperature, i.e.,

$U=U_{\mathrm{nf}}=V=V_{\mathrm{nf}}=\Psi=0$, $\Theta=0$, at $X=0$, 1 and $Y=0$, 1

(1) The circle surface is maintained at a constant hot temperature, i.e.,

$$U=U_{\mathrm{nf}}=V=V_{\mathrm{nf}}=\Psi=0,\quad \Theta=1$$

(2) At the interface, the boundary conditions are derived from equating (continuity) of tangential and normal velocities, shear and normal stresses, temperature, and the heat flux across the interface. Hence, the interface conditions can be written as follows [20]:

$$\left.\begin{aligned}
&\theta=\theta_{\mathrm{nf}};\ \frac{\partial\theta}{\partial X}=R_k\frac{\partial\theta_{\mathrm{nf}}}{\partial X}\\
&\psi=\psi_{\mathrm{nf}};\ \frac{\partial\psi}{\partial X}=\frac{\partial\psi_{\mathrm{nf}}}{\partial X}\\
&\mu_{\mathrm{np}}\left(\frac{\partial U}{\partial Y}+\frac{\partial V}{\partial X}\right)=\mu_{\mathrm{nf}}\left(\frac{\partial U_{\mathrm{nf}}}{\partial Y}+\frac{\partial V_{\mathrm{nf}}}{\partial X}\right)\\
&P=P_{\mathrm{nf}};\ \frac{\partial P}{\partial X}=\frac{\partial P_{\mathrm{nf}}}{\partial X}
\end{aligned}\right\}\ \text{at } X=X_p \text{ and } 0\le Y\le 1$$

4 Numerical Solution

The dimensionless governing equations that are described are discretized and solved by using the Galerkin finite element method to get the temperature with the stream function.

The continuity Eqs. (17) and (21) will be used as a constraint due to mass conservation, and this constraint may be used to obtain the pressure distribution [33]. In order to solve Eqs. (18), (19), (23), and (24), the penalty finite element method (FEM) is used where the pressure P is eliminated by a penalty parameter $\mathfrak{r}$ and the incompressibility criteria are given by Zhang et al. [25], which results in

$$P=-\mathfrak{r}\left(\frac{\partial U}{\partial X}+\frac{\partial V}{\partial Y}\right)P=-\mathfrak{r}\left(\frac{\partial U_{\mathrm{nf}}}{\partial X}+\frac{\partial V_{\mathrm{nf}}}{\partial Y}\right) \tag{28}$$

Using Eqs. (17) and (21), the momentum balance equations reduce to

$$U\frac{\partial U}{\partial X}+V\frac{\partial U}{\partial Y}=\mathfrak{r}\frac{\partial}{\partial X}\left(\frac{\partial U}{\partial X}+\frac{\partial V}{\partial Y}\right)+\frac{\mathrm{Pr}}{(1-\phi)^{2.5}}\frac{\rho_f}{\rho_{\mathrm{nf}}}\left(\frac{\partial^2 U}{\partial X^2}+\frac{\partial^2 U}{\partial Y^2}\right)-\frac{\mathrm{Pr}}{(1-\phi)^{2.5}}\frac{\rho_f}{\rho_{\mathrm{nf}}}\frac{U}{\mathrm{Da}} \tag{29}$$

$$U\frac{\partial V}{\partial X}+V\frac{\partial V}{\partial Y}=\mathfrak{r}\frac{\partial}{\partial Y}\left(\frac{\partial U}{\partial X}+\frac{\partial V}{\partial Y}\right)+\frac{\mathrm{Pr}}{(1-\phi)^{2.5}}\frac{\rho_f}{\rho_{\mathrm{nf}}}\left(\frac{\partial^2 V}{\partial X^2}+\frac{\partial^2 V}{\partial Y^2}\right)-\frac{\mathrm{Pr}}{(1-\phi)^{2.5}}\frac{\rho_f}{\rho_{\mathrm{nf}}}\frac{V}{\mathrm{Da}}+\frac{(\rho\beta)_{\mathrm{nf}}}{\rho_{\mathrm{nf}}\beta_f}\mathrm{RaPr}\Theta \tag{30}$$

$$U_{\mathrm{nf}}\frac{\partial U_{\mathrm{nf}}}{\partial X}+V\frac{\partial U_{\mathrm{nf}}}{\partial Y}=\mathfrak{r}\frac{\partial}{\partial X}\left(\frac{\partial U_{\mathrm{nf}}}{\partial X}+\frac{\partial V_{\mathrm{nf}}}{\partial Y}\right)+\frac{\mathrm{Pr}}{(1-\phi)^{2.5}}\frac{\rho_f}{\rho_{\mathrm{nf}}}\left(\frac{\partial^2 U_{\mathrm{nf}}}{\partial X^2}+\frac{\partial^2 U_{\mathrm{nf}}}{\partial Y^2}\right) \tag{31}$$

$$V_{\mathrm{nf}}\frac{\partial V_{\mathrm{nf}}}{\partial X}+V\frac{\partial V_{\mathrm{nf}}}{\partial Y}=\mathfrak{r}\frac{\partial}{\partial Y}\left(\frac{\partial U_{\mathrm{nf}}}{\partial X}+\frac{\partial V_{\mathrm{nf}}}{\partial Y}\right)+\frac{\mathrm{Pr}}{(1-\phi)^{2.5}}\frac{\rho_f}{\rho_{\mathrm{nf}}}\left(\frac{\partial^2 V_{\mathrm{nf}}}{\partial X^2}+\frac{\partial^2 V_{\mathrm{nf}}}{\partial Y^2}\right)+\frac{(\rho\beta)_{\mathrm{nf}}}{\rho_{\mathrm{nf}}\beta_f}\mathrm{Ra}\,\mathrm{Pr}\,\Theta \tag{32}$$

In order to obtain a weak formulation for the problem defined by Eqs. (20), (24), and (29)–(32), the momentum and energy equations are multiplied by a shape function (φ) and integrated over the domain D. Thus, we get

$$\int_\Omega \left(\varphi_i U^h \frac{\partial U^h}{\partial X} + \varphi_i V^h \frac{\partial U^h}{\partial Y}\right) dXdY = \aleph \int_\Omega \frac{\partial \varphi_i}{\partial X}\left(\frac{\partial U^h}{\partial X} + \frac{\partial V^h}{\partial Y}\right) dXdY + \frac{\Pr}{(1-\phi)^{2.5}} \frac{\rho_f}{\rho_{\rm nf}} \int_\Omega \varphi_i \left(\frac{\partial^2 U^h}{\partial X^2} + \frac{\partial^2 U^h}{\partial Y^2}\right) dXdY - \frac{\Pr}{(1-\phi)^{2.5}} \frac{\rho_f}{\rho_{\rm nf}} \frac{1}{\rm Da} \int_\Omega \varphi_i U^h dXdY \tag{33}$$

$$\int_\Omega \left(\varphi_i U^h \frac{\partial V^h}{\partial X} + \varphi_i V^h \frac{\partial V^h}{\partial Y}\right) dXdY = \aleph \int_\Omega \frac{\partial \varphi_i}{\partial Y}\left(\frac{\partial U^h}{\partial X} + \frac{\partial V^h}{\partial Y}\right) dXdY + \frac{\Pr}{(1-\phi)^{2.5}} \frac{\rho_f}{\rho_{\rm nf}} \int_\Omega \varphi_i \left(\frac{\partial^2 V^h}{\partial X^2} + \frac{\partial^2 V^h}{\partial Y^2}\right) dXdY - \frac{\Pr}{(1-\phi)^{2.5}} \frac{\rho_f}{\rho_{\rm nf}} \frac{1}{\rm Da} \int_\Omega \varphi_i V^h dXdY + \frac{(\rho\beta)_{nf}}{\rho_{\rm nf}\beta_f} {\rm RaPr} \int_\Omega \varphi_i \Theta^h dXdY \tag{34}$$

$$\int_\Omega \left(\varphi_i U^h_{\rm nf} \frac{\partial U^h_{\rm nf}}{\partial X} + \varphi_i V^h_{\rm nf} \frac{\partial U^h_{\rm nf}}{\partial Y}\right) dXdY = \aleph \int_\Omega \frac{\partial \varphi_i}{\partial X}\left(\frac{\partial U^h_{\rm nf}}{\partial X} + \frac{\partial V^h_{\rm nf}}{\partial Y}\right) dXdY + \frac{\Pr}{(1-\phi)^{2.5}} \frac{\rho_f}{\rho_{\rm nf}} \int_\Omega \varphi_i \left(\frac{\partial^2 U^h_{\rm nf}}{\partial X^2} + \frac{\partial^2 U^h_{\rm nf}}{\partial Y^2}\right) dXdY \tag{35}$$

$$\int_\Omega \left(\varphi_i U^h_{\rm nf} \frac{\partial V^h_{\rm nf}}{\partial X} + \varphi_i V^h_{\rm nf} \frac{\partial V^h_{\rm nf}}{\partial Y}\right) dXdY = \aleph \int_\Omega \frac{\partial \varphi_i}{\partial Y}\left(\frac{\partial U^h_{\rm nf}}{\partial X} + \frac{\partial V^h_{\rm nf}}{\partial Y}\right) dXdY + \frac{\Pr}{(1-\phi)^{2.5}} \frac{\rho_f}{\rho_{\rm nf}} \int_\Omega \varphi_i \left(\frac{\partial^2 V^h_{\rm nf}}{\partial X^2} + \frac{\partial^2 V^h_{\rm nf}}{\partial Y^2}\right) dXdY + \frac{(\rho\beta)_{\rm nf}}{\rho_{\rm nf}\beta_f} {\rm RaPr} \int_\Omega \varphi_i \Theta^h_{\rm nf} dXdY \tag{36}$$

$$\int_\Omega \left(\varphi_i U^h \frac{\partial \Theta^h}{\partial X} + \varphi_i V^h \frac{\partial \Theta^h}{\partial Y}\right) dxdy = \frac{\alpha_{\rm nf}}{\alpha_f} \int_\Omega \varphi_i \left(\frac{\partial^2 \Theta^h}{\partial X^2} + \frac{\partial^2 \Theta^h}{\partial Y^2}\right) dxdy \tag{37}$$

$$\int_\Omega \left(\varphi_i U^h_{\rm nf} \frac{\partial \Theta^h_{\rm nf}}{\partial X} + \varphi_i V^h_{\rm nf} \frac{\partial \Theta^h_{\rm nf}}{\partial Y}\right) dxdy = \frac{\alpha_{\rm nf}}{\alpha_f} \int_\Omega \varphi_i \left(\frac{\partial^2 \Theta^h_{\rm nf}}{\partial X^2} + \frac{\partial^2 \Theta^h_{\rm nf}}{\partial Y^2}\right) dxdy \tag{38}$$

The first step in applying the FEM to the weak form given by Eqs. (34)–(38) is to discretize the domain (D) into a finite number of subdomains. The domain (D) is appears by internal domain (Ω), and the domain (Ω) belongs to the double integrals ($dXdY$).

The approximate velocity components and the temperature are

$$\begin{aligned} U^h &= \sum_{k=1}^n U_k \varphi_k V^h = \sum_{k=1}^n V_k \varphi_k U^h_{\rm nf} = \sum_{k=1}^n U_{{\rm nf}k} \varphi_k V^h_{\rm nf} = \sum_{k=1}^n V_{{\rm nf}k} \varphi_k \\ \Theta^h &= \sum_{k=1}^n \Theta_k \varphi_k \Theta^h_{\rm nf} = \sum_{k=1}^n \Theta_{{\rm nf}k} \varphi_k \end{aligned} \tag{39}$$

The Galerkin finite element method yields the following nonlinear residual equations for Eqs. (34)–(38), at nodes of internal domain (Ω):

$$R_i^{(1)} = \sum_{k=1}^n U_k \int_\Omega \left[\left(\sum_{k=1}^n U_k \varphi_k\right)\frac{\partial \varphi_k}{\partial X} + \left(\sum_{k=1}^n V_k \varphi_k\right)\frac{\partial \varphi_k}{\partial Y}\right]\varphi_i dXdY + \aleph\left[\sum_{k=1}^n U_k \int_\Omega \frac{\partial \varphi_i}{\partial X}\frac{\partial \varphi_k}{\partial X} dXdY + \sum_{k=1}^n V_k \int_\Omega \frac{\partial \varphi_i}{\partial X}\frac{\partial \varphi_k}{\partial Y} dXdY\right] + \frac{\Pr}{(1-\phi)^{2.5}} \frac{\rho_f}{\rho_{\rm nf}} \sum_{k=1}^n U_k \int_\Omega \left[\frac{\partial \varphi_i}{\partial X}\frac{\partial \varphi_k}{\partial X} + \frac{\partial \varphi_i}{\partial Y}\frac{\partial \varphi_k}{\partial Y}\right] dXdY + \frac{\Pr}{(1-\phi)^{2.5}} \frac{\rho_f}{\rho_{\rm nf}} \frac{1}{\rm Da} \int_\Omega \left(\sum_{k=1}^n U_k \varphi_k\right)\varphi_i dXdY \tag{40}$$

$$R_i^{(2)} = \sum_{k=1}^n V_k \int_\Omega \left[\left(\sum_{k=1}^n U_k \varphi_k\right)\frac{\partial \varphi_k}{\partial X} + \left(\sum_{k=1}^n V_k \varphi_k\right)\frac{\partial \varphi_k}{\partial Y}\right]\varphi_i dXdY + \aleph\left[\sum_{k=1}^n U_k \int_\Omega \frac{\partial \varphi_i}{\partial Y}\frac{\partial \varphi_k}{\partial X} dXdY + \sum_{k=1}^n V_k \int_\Omega \frac{\partial \varphi_i}{\partial Y}\frac{\partial \varphi_k}{\partial Y} dXdY\right] + \frac{\Pr}{(1-\phi)^{2.5}} \frac{\rho_f}{\rho_{\rm nf}} \sum_{k=1}^n V_k \int_\Omega \left[\frac{\partial \varphi_i}{\partial X}\frac{\partial \varphi_k}{\partial X} + \frac{\partial \varphi_i}{\partial Y}\frac{\partial \varphi_k}{\partial Y}\right] dXdY + \frac{\Pr}{(1-\phi)^{2.5}} \frac{\rho_f}{\rho_{\rm nf}} \frac{1}{\rm Da} \int_\Omega \left(\sum_{k=1}^n V_k \varphi_k\right)\varphi_i dXdY - \frac{(\rho\beta)_{\rm nf}}{\rho_{\rm nf}\beta_f} {\rm RaPr} \int_\Omega \left(\sum_{k=1}^n \Theta_k \varphi_k\right)\varphi_i dXdY \tag{41}$$

$$R_i^{(3)} = \sum_{k=1}^n U_{{\rm nf}k} \int_\Omega \left[\left(\sum_{k=1}^n U_{{\rm nf}k} \varphi_k\right)\frac{\partial \varphi_k}{\partial X} + \left(\sum_{k=1}^n V_{{\rm nf}k} \varphi_k\right)\frac{\partial \varphi_k}{\partial Y}\right]\varphi_i dXdY + \aleph\left[\sum_{k=1}^n U_{{\rm nf}k} \int_\Omega \frac{\partial \varphi_i}{\partial X}\frac{\partial \varphi_k}{\partial X} dXdY + \sum_{k=1}^n V_{nf_k} \int_\Omega \frac{\partial \varphi_i}{\partial X}\frac{\partial \varphi_k}{\partial Y} dXdY\right] + \frac{\Pr}{(1-\phi)^{2.5}} \frac{\rho_f}{\rho_{\rm nf}} \sum_{k=1}^n U_{{\rm nf}k} \int_\Omega \left[\frac{\partial \varphi_i}{\partial X}\frac{\partial \varphi_k}{\partial X} + \frac{\partial \varphi_i}{\partial Y}\frac{\partial \varphi_k}{\partial Y}\right] dXdY \tag{42}$$

$$R_i^{(4)} = \sum_{k=1}^{n} V_{\mathrm{nf}k} \int_\Omega \left[\left(\sum_{k=1}^{n} U_{\mathrm{nf}k}\varphi_k \right) \frac{\partial \varphi_k}{\partial X} + \left(\sum_{k=1}^{n} V_{\mathrm{nf}k}\varphi_k \right) \frac{\partial \varphi_k}{\partial Y} \right] \varphi_i dXdY + \aleph \left[\sum_{k=1}^{n} U_{\mathrm{nf}k} \int_\Omega \frac{\partial \varphi_i}{\partial Y}\frac{\partial \varphi_k}{\partial X} dXdY + \sum_{k=1}^{n} V_{\mathrm{nf}k} \int_\Omega \frac{\partial \varphi_i}{\partial Y}\frac{\partial \varphi_k}{\partial Y} dXdY \right] + \frac{\mathrm{Pr}}{(1-\phi)^{2.5}} \frac{\rho_f}{\rho_{\mathrm{nf}}} \sum_{k=1}^{n} V_{\mathrm{nf}k} \int_\Omega \left[\frac{\partial \varphi_i}{\partial X}\frac{\partial \varphi_k}{\partial X} + \frac{\partial \varphi_i}{\partial Y}\frac{\partial \varphi_k}{\partial Y} \right] dXdY - \frac{(\rho\beta)_{\mathrm{nf}}}{\rho_{\mathrm{nf}}\beta_f} \mathrm{RaPr} \int_\Omega \left(\sum_{k=1}^{n} \Theta_k \varphi_k \right) \varphi_i dXdY \tag{43}$$

$$R_i^{(5)} = \sum_{k=1}^{n} \Theta_k \int_\Omega \left[\left(\sum_{k=1}^{n} U_k \varphi_k \right) \frac{\partial \varphi_k}{\partial X} + \left(\sum_{k=1}^{n} V_k \varphi_k \right) \frac{\partial \varphi_k}{\partial Y} \right] \varphi_i dXdY + \frac{\alpha_{\mathrm{nf}}}{\alpha_f} \sum_{k=1}^{n} \Theta_k \left[\int_\Omega \frac{\partial \varphi_i}{\partial X}\frac{\partial \varphi_k}{\partial X} dXdY + \int_\Omega \frac{\partial \varphi_i}{\partial Y}\frac{\partial \varphi_k}{\partial Y} dXdY \right] \tag{44}$$

$$R_i^{(6)} = \sum_{k=1}^{n} \Theta_{\mathrm{nf}k} \int_\Omega \left[\left(\sum_{k=1}^{n} U_{\mathrm{nf}k}\varphi_k \right) \frac{\partial \varphi_k}{\partial X} + \left(\sum_{k=1}^{n} V_{\mathrm{nf}k}\varphi_k \right) \frac{\partial \varphi_k}{\partial Y} \right] \varphi_i dXdY + \frac{\alpha_{\mathrm{nf}}}{\alpha_f} \sum_{k=1}^{n} \Theta_{\mathrm{nf}k} \left[\int_\Omega \frac{\partial \varphi_i}{\partial X}\frac{\partial \varphi_k}{\partial X} dXdY + \int_\Omega \frac{\partial \varphi_i}{\partial Y}\frac{\partial \varphi_k}{\partial Y} dXdY \right] \tag{45}$$

4.1 Finite Element Discretization for Stream Function. Applying the weak formation analysis

$$\int_D \varphi \left(\frac{\partial}{\partial X}\frac{\partial \psi}{\partial X} + \frac{\partial}{\partial Y}\frac{\partial \psi}{\partial Y} \right) dD = \int_D \varphi \left(\frac{\partial U}{\partial Y} - \frac{\partial V}{\partial X} \right) dD \tag{46}$$

$$\int_D \varphi \left(\frac{\partial}{\partial X}\frac{\partial \psi_{nf}}{\partial X} + \frac{\partial}{\partial Y}\frac{\partial \psi_{nf}}{\partial Y} \right) dD = \int_D \varphi \left(\frac{\partial U_{\mathrm{nf}}}{\partial Y} - \frac{\partial V_{\mathrm{nf}}}{\partial X} \right) dD \tag{47}$$

When the approximate stream function is

$$\psi = \sum_{k=1}^{n} \psi_k \varphi_k \quad \psi_{\mathrm{nf}} = \sum_{k=1}^{n} \psi_{\mathrm{nf})_k} \varphi_k \tag{48}$$

The Galerkin finite element method yields the following nonlinear residual equations for stream function and can be written as follows:

$$R_i^s = \sum_{k=1}^{n} \psi_k \int_\Omega \left[\frac{\partial \varphi_i}{\partial X}\frac{\partial \varphi_k}{\partial X} + \frac{\partial \varphi_i}{\partial Y}\frac{\partial \varphi_k}{\partial Y} \right] dXdY + \sum_{k=1}^{n} U_k \int_\Omega \varphi_i \frac{\partial \varphi_k}{\partial Y} dXdY - \sum_{k=1}^{n} V_k \int_\Omega \varphi_i \frac{\partial \varphi_k}{\partial X} dXdY \tag{49}$$

$$R_{\mathrm{nf})_i}^s = \sum_{k=1}^{n} \psi_{\mathrm{nf})_k} \int_\Omega \left[\frac{\partial \varphi_i}{\partial X}\frac{\partial \varphi_k}{\partial X} + \frac{\partial \varphi_i}{\partial Y}\frac{\partial \varphi_k}{\partial Y} \right] dXdY + \sum_{k=1}^{n} U_{\mathrm{nf})_k} \int_\Omega \varphi_i \frac{\partial \varphi_k}{\partial Y} dXdY - \sum_{k=1}^{n} V_{\mathrm{nf})_k} \int_\Omega \varphi_i \frac{\partial \varphi_k}{\partial X} dXdY \tag{50}$$

4.2 Finite Element Discretization for Local and Average Nusselt Numbers. The average Nusselt number for hot left wall of enclosure can also be written in a nondimensional form as follows:

$$\mathrm{Nu} = \frac{k_{\mathrm{nf}}}{k_f}\frac{1}{\pi}\frac{\partial \Theta}{\partial n} \quad \overline{\mathrm{Nu}} = \frac{k_{\mathrm{nf}}}{k_f} \int_0^1 \frac{\partial \Theta}{\partial n} dY \tag{51}$$

We assume the dimensionless temperature for normal vector expresses as follows:

$$\frac{\partial \Theta}{\partial n} = \sqrt[2]{\left(\frac{\partial \Theta}{\partial X} \right)^2 + \left(\frac{\partial \Theta}{\partial Y} \right)^2} \tag{52}$$

The FEM distribution can be applied as follow:

$$\mathrm{Nu} = \frac{k_{\mathrm{nf}}}{k_f}\frac{1}{\pi} \sum_{j=1}^{m} \Theta_j \sqrt[2]{\left(\frac{\partial \phi_j}{\partial X} \right)^2 + \left(\frac{\partial \phi_j}{\partial Y} \right)^2} \tag{53}$$

$$\overline{\mathrm{Nu}} = \frac{k_{\mathrm{nf}}}{k_f}\frac{1}{\pi} \sum_{j=1}^{m} \Theta_j \int_0^\pi \sqrt[2]{\left(\frac{\partial \varphi_j}{\partial X} \right)^2 + \left(\frac{\partial \varphi_j}{\partial Y} \right)^2} d\zeta \tag{54}$$

5 Grid Independent Test

In order to solve the problem with low computation time and high accuracy, a test is made to search for the minimum number of elements that leads to grid-independent solution. Grid independence study was performed to obtain an appropriate grid distribution with accurate results and minimal computational time. The averaged Nusselt number results for various grid sizes are shown in Table 1 at $\mathrm{Ra} = 10^6$, $\mathrm{Da} = 0.1$, $X_p = 0.2$, and $\varphi = 0.1$.

Table 1 Grid independence test results for different geometries of the inner cylinder at $\mathrm{Ra} = 10^6$, $\mathrm{Da} = 0.1$, $X_p = 0.2$, and $\varphi = 0.1$

Circle		Triangle	
No. of elements	$\overline{\mathrm{Nu}}$	No. of elements	$\overline{\mathrm{Nu}}$
830	16.970	1473	15.873
1272	17.057	2181	18.852
2002	18.097	3506	19.897
6762	20.096	9626	22.025
19,878	20.111	18,774	22.025

Elliptic		Rectangle		Rhombic	
No. of elements	$\overline{\mathrm{Nu}}$	No. of elements	$\overline{\mathrm{Nu}}$	No. of elements	$\overline{\mathrm{Nu}}$
1010	14.327	1654	13.931	1552	16.272
1406	16.299	2454	15.768	2424	17.378
2190	18.305	3882	18.431	3876	19.471
6788	22.256	10,120	20.864	4970	21.618
19,780	22.256	26,608	20.863	22,270	21.618

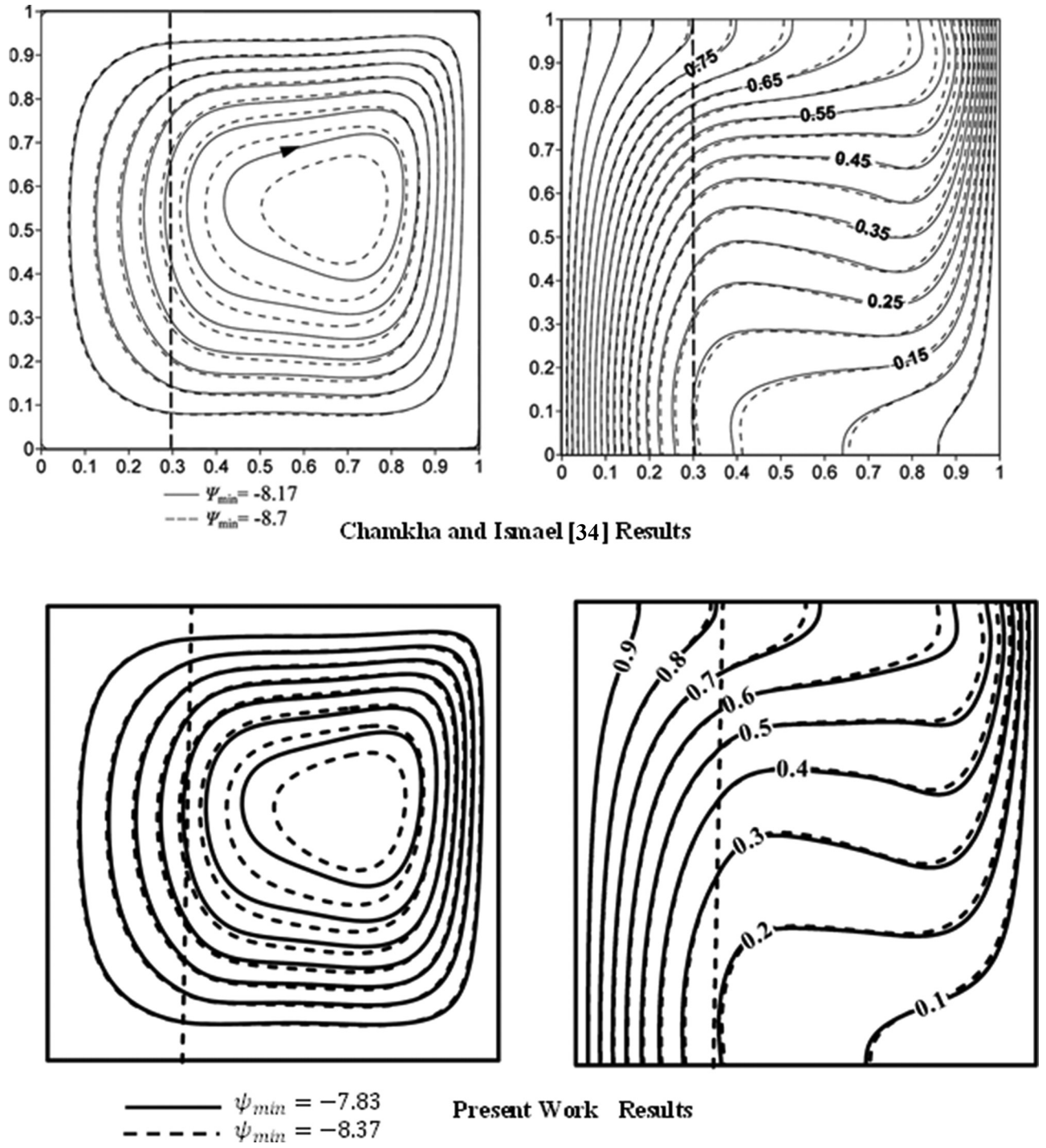

Fig. 2 Streamlines on the left and isotherms on the right, for a square cavity with hot left sidewall and cold right sidewall and adiabatic top and bottom walls at Ra = 10^5, Da = 10^{-5}, $\delta = 0$, $A = 1$, $X_p = 0.3$, $\varphi = 0$ (solid lines) and $\varphi = 0.05$ (dashed lines) with the corresponding results of benchmark problem [34] (Reproduced with permission of Taylor & Francis, Ltd., copyright 2014)

Table 2 Thermophysical properties of base fluid (pure water) and nanoparticles [30]

Properties	Pure water	Silver (Ag)
C_p (J/kg K)	4179	235
K (W/m K)	0.613	429
ρ (kg/m^3)	997.1	10,500
β (1/K) $\times 10^{-5}$	21	1.89

6 Validation of the Results

In this work, two researches have been testing to validate the results of the developed numerical code. First research relates with the heat transfer and fluid flow for nanofluid inside a square cavity having hot solid block [32]. The comparison is carried out using the following dimensionless parameters: Pr = 6.82 and $\varphi = 0.03$ for $l/L = 0.2$ and $h/L = 0.25$. The second research relates with the heat transfer and fluid flow in two-layer system that includes a porous media and nanofluid inside the square enclosure [34] with vertical interface between the nanofluid and porous

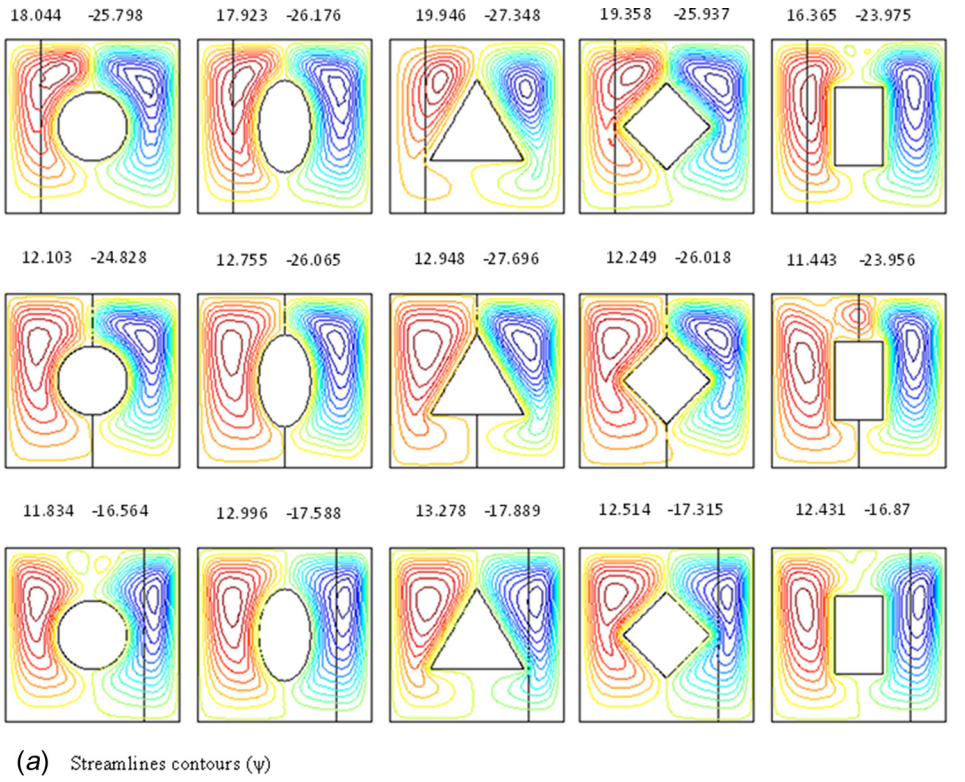

Fig. 3 Streamlines contours (ψ) and isotherm contours (θ) of saturated porous-nanofluid (left layer) and the same nanofluid (right layer) for ((*a*) $X_p = 20\%$ upper row, (*b*) $X_p = 50\%$ middle row, and (*c*) $X_p = 80\%$ lower row) and ($Ra = 10^6$, $\varphi = 0.05$, $R_k = 1$ and $Da = 10^{-3}$)

layers at ($Ra = 10^5$, $Da = 10^{-5}$, $A = 1$, $X_p = 0.3$, $\varphi = 0$ (solid lines) and $\varphi = 0.05$ (dashed lines)). The comparison for both problems is in excellent agreement between the previous and present results as shown in Fig. 3, respectively, which provide sufficient confidence in the present numerical algorithm.

7 Results and Discussion

In the present problem, the natural convection in a differentially heated between a cold outer square enclosure and hot inner cylinder in two domain system (porous/nanofluid and nanofluid) is investigated numerically using the Galerkin finite element method. The nanofluid is considered to be composed of water base fluid ($Pr = 6.2$) and Ag nanoparticles (with physical properties shown in Table 2). The ranges of the studied parameters are as follows: $X_p = 0$–100%, $Ra = 10^3$–10^6, $Da = 10^{-5}$–10^{-1}, $R_k = 1$–20, and $\varphi = 0$–0.1.

Figure 3 shows the streamlines contours (ψ) and isotherm contours (θ) of saturated porous-nanofluid (left layer) and the same nanofluid (right layer) for various values of thickness the porous

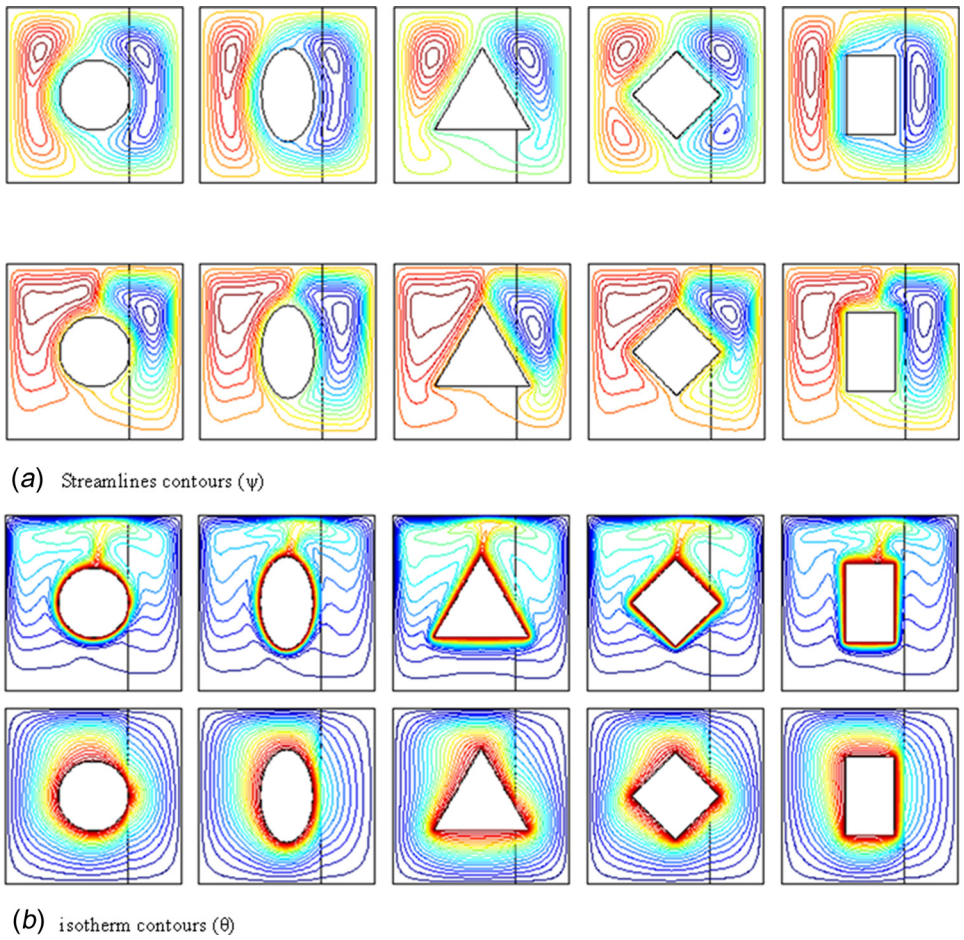

Fig. 4 Streamline contours (ψ) and isotherm contours (θ) of saturated porous-nanofluid (left layer) and the same nanofluid (right layer) for ((*a*) $Ra = 10^3$ upper row and (*b*) $Ra = 10^6$ lower row) and ($X_p = 0.7$, $\varphi = 0.1$, $R_k = 5$, and $Da = 0.01$)

layer and ($Ra = 10^6$, $\varphi = 0.05$, $R_k = 1$ and $Da = 10^{-3}$) for five different geometries of internal hot cylinder (i.e., circular, elliptic, triangular, rhombic, and rectangular).

In general, it can be noted that there are two longitudinal vortices for all cases of the internal cylinder. The distribution of the streamlines Fig. 3(*a*) is at a stable state in the triangular cylinder because of the availability of sufficient space for thermal convection in the upper half of the enclosure. This can be observed from the maximum values of the stream function which decrease from $\psi_{max} = -25.798, -26.176, -27.348, -25.937$, and -23.975 at ($X_p = 20\%$) to $\psi_{max} = -16.563, -17.588, -17.889, -17.315$, and -16.87 at ($X_p = 80\%$) for circle, elliptic, triangle, rhombic and rectangle, respectively. When the thickness of the porous layer is increased, the free convection performance will decrease significantly (to about 50%) due to the hydrodynamic properties of the porous material, where the interrelated pores work to slow down and inhibit the flow of nanofluid. Also, it can be observed that when the thickness of the porous layer increases, the two vortices will become more longitudinal.

With respect to the isotherms, it can be seen in Fig. 3(*b*) that the isotherms are clustered near the heat source location (surface cylinder) due to the severe effect of the convection that decreases gradually toward the cold sidewalls. The shape of isotherms is not much changed due to tough effect of natural convection because of the high Rayleigh number. Figure 4 shows the streamline contours (ψ) and isotherm contours (θ) of saturated porous-nanofluid (left layer) and the same nanofluid (right layer) for various values of Rayleigh number and ($X_p = 0.7$, $\varphi = 0.1$, $R_k = 5$, and $Da = 0.01$). Figure 5(*a*) depicts the distribution of the streamlines which means an increase in the Rayleigh number increases the normal convection activity due to the increase in the buoyancy force. Therefore, the increase in the normal convection activity causes an increase in the rate of transmission of heat transferred to normal convection resulting from increased temperature decline. Where the lines of the stream function are almost identical around the center of the gap while the temperature distribution lines are almost vertical when the value of the Rayleigh number is low. The increase in the Rayleigh number leads to asymmetry in the lines around the center and moving the temperature lines toward the upper wall as the lines of the stream function of the inner cylinder by increasing the value of the Rayleigh number indicates the increase in the flow velocity near this cylinder, while it decreases near the bottom wall of the enclosure. For temperatures, the movement of temperature lines toward the upper wall is indicative of the effect of the load shown by increasing the Rayleigh number. With respect to the isotherm, Fig. 4(*b*) represents the temperature change along the symmetry line, where we observe an increase in the value of the dimensionless temperature at each value of Rayleigh number. Increasing the Rayleigh number leads to reduce the dimensionless temperature beyond the maximum values as the mechanism of heat transfer becomes a convection instead of conduction. Figure 5 manifests the streamline contours (ψ) and isotherm contours (θ) of saturated porous-nanofluid (lower layer) and the same nanofluid (left layer) for various values of Darcy number and ($X_p = 0.4$, $\varphi = 0.07$, $R_k = 20$, and $Ra = 10^5$). It can be noted that when the Darcy number increases, the activity of normal convection in the left layer of the enclosure

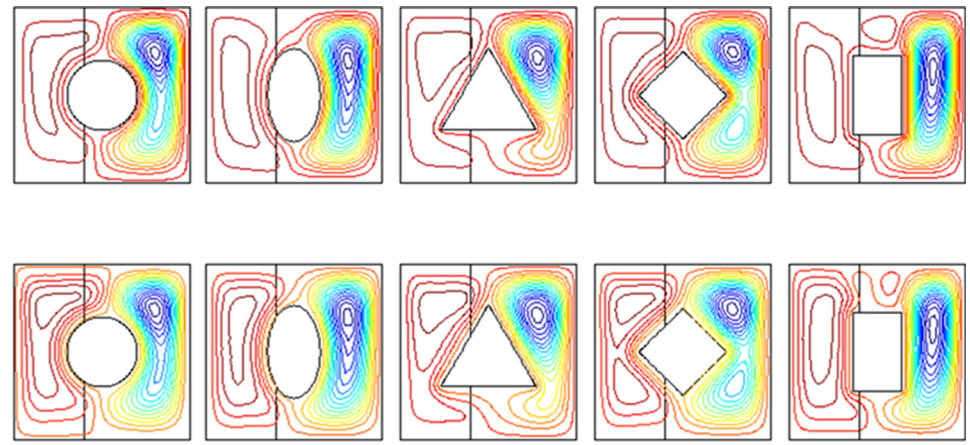

Fig. 5 Streamline contours (ψ) and isotherm contours (θ) of saturated porous-nanofluid (left layer) and the same nanofluid (right layer) for ((*a*) $Da = 10^{-3}$ upper row and (*b*) $Da = 0.1$ lower row) and ($X_p = 0.4$, $\varphi = 0.07$, $R_k = 20$ and $Ra = 10^5$)

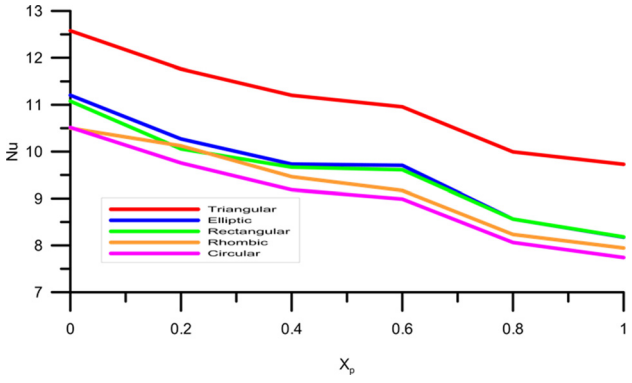

Fig. 6 Profile of average Nusselt number along the hot cylinder surface with thickness of porous layer for different values of Darcy number and ($Da = 10^{-3}$, $\varphi = 0.05$, $Ra = 10^5$)

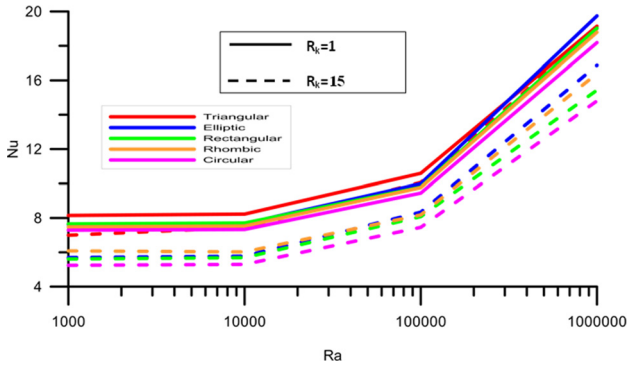

Fig. 7 Profile of the average Nusselt number along the hot cylinder surface with Rayleigh number for ($R_k = 1$ solid lines), ($R_k = 10$ dashed lines) and ($Da = 10^{-3}$, $X_p = 0.3$, $\varphi = 0.05$)

(the porous layer saturated with nanofluid) will increase Fig. 5(*a*). The absolute value of the maximum stream function increases with increasing the Darcy number, for example it increases from ($\psi_{min} = 0.8647, 0.7197, 0.7977, 0.7476, 0.6765$) at ($Da = 10^{-3}$) to ($\psi_{min} = 2.1189, 2.0458, 1.7252, 2.0189, 1.5266$) at ($Da = 0.1$). This is due to the fact that increasing the Darcy number will lead to increased permeability in the porous layer and, therefore, allowing more nanofluids to penetrate the porous layer. As a result, cell strength is increased significantly. With respect to isotherms, it can be seen in Fig. 5(*b*) that when the Darcy number is low ($Da = 10^{-3}$), isotherm lines are generally distributed vertically. This is due to the low effect of convection at law Darcy number; in this case, the heat transfer by conduction is dominant. However, when the Darcy number is high ($Da = 0.1$), a clear change can be seen in the form of isotherm. It changes its shape from vertical to horizontal. In this case, heat is transferred into the convection.

The amount of heat transfer can be deduced from the knowledge of the change in the Nusselt number as a result of changing the parameters of the study. Figure 6 shows the effect of changing the thickness of the porous layer and ($Da = 10^{-3}$ $\varphi = 0.05$

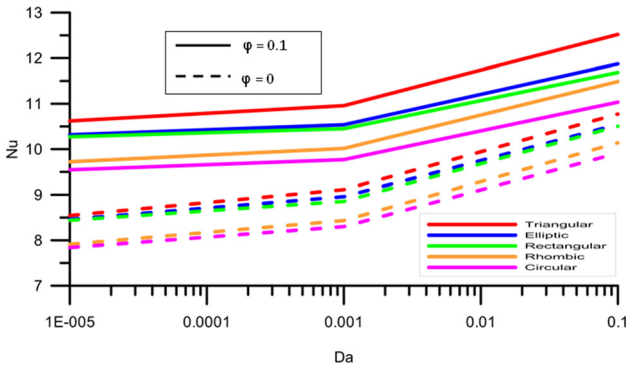

Fig. 8 Profile of the average Nusselt number along the hot cylinder surface with Darcy number for with ($\varphi = 0.1$ solid lines), ($\varphi = 0$ dashed lines) and ($X_p = 0.6$, Ra $= 10^5$, $R_k = 1$)

$\mathrm{Ra} = 10^5$). Where it is noted that the progress or increase in the thickness of the porous layer will lead to a clear drop in the amount of Nusselt number of all cases of the cylinder. This decreasing in the Nusselt number value occurs due to the binding and restriction of nanoparticle particles on the side of the porous layer, and thus note the dominance of heat transfer by conduction, which is likely to decrease the Nusselt number product.

Figure 7 shows the profile of average Nusselt numbers along the heat source (surface cylinder) with ($R_k = 1$ solid lines), ($R_k = 10$ dashed lines), and for ($\mathrm{Da} = 10^{-3}$, $X_p = 0.3$, $\varphi = 0.05$). It is interesting to note that an increase in the Nusselt number for all cases is accompanied by an increase in the Ra number of different values of thermal conductivity. The remarkable object that can be drawn from Figure 8 is that the difference in the increasing value of the Nusselt number of the surface internal cylinder is a low in the Ra number low when changing the thermal connection and when increasing the Ra number, we notice a great difference in the increase in the rate of the Nusselt number of changes in thermal conductivity. As we observe the increase in the Nusselt number values by increasing the thermal conductivity, i.e., in the case of approaching the state of thermal equilibrium, the highest rate of the Nusselt value occurs. Figure 8 shows the profile of local Nusselt number along the heat source (surface cylinder) with ($\varphi = 0.1$ solid lines), ($\varphi = 0$ dashed lines), and for ($X_p = 0.6$ $\mathrm{Ra} = 10^5$ $R_k = 1$). It is noted from the figure that the Nusselt number is not much affected by the change in the coefficient of heat transfer listed at the range (10^{-5}–10^{-3}), i.e., when the Darcy number is low. The rate of the Nusselt number for the period (10^{-3}–0.1) is more responsive to that change, as the rate of the Nusselt number of the steel section is increased by increasing the coefficient of heat transfer listed to increase the amount of heat exchange. When the nanoparticle's volume fraction is increased, we will observe an increase in the Nusselt number and in all cases of the cylinder. Also, it can be seen from Fig. 8 that the value of Nusselt number increases when the volume fraction increases; this is because increasing φ leads to an increase in the thermal conductivity, viscosity, and density of the nanofluid in two-layer enclosure. Therefore, it is concluded from Fig. 8 that the rate of heat transfer increases when φ increases.

8 Conclusions

Natural convection heat transfer induced by a temperature difference between a hot inner cylinder with different geometries (i.e., circular; triangular; elliptic; rectangular; and rhombic) and a cold outer square enclosure and partially porous cavity filled with a nanofluid was analyzed numerically based on the Galerkin finite element method formulation. The main feature of this study was to determine if the conventional studied parameters in partially porous cavity like the permeability and the thickness of porous layer, the thermal conductivity, Rayleigh number, the thermal conductivity ratio, and the best inner geometry concerned with the best improvement of natural convection are determined by the volume fraction of the nanoparticles. Therefore, combinations of six parameter effects were studied. The main derived remarks from the present results were as follows: It has been observed that with the increase of the Rayleigh number, Darcy number, thermal conductivity ratio, and the nanoparticle volume fraction, the intensity of the fluid flow and the convection heat transfer increase, while they decrease when the thickness of porous layer increases. While the isotherm lines become more curved as the Rayleigh number, Darcy number, thermal conductivity ratio, and volume fraction increase, whereas a reverse behavior can be seen when the thickness of porous layer increases. Also, it can be concluded from the results that the best improvement of natural convection is in the triangular cylinder shape. Moreover, it can be concluded that when the thickness of the porous layer is increased from 20% to 80%, the free convection performance will decrease significantly (to about 50%) due to the hydrodynamic properties of the porous material. The results depicted that the average Nusselt number values are lower than (60–70%) from its value when the enclosure included overall saturated porous media.

Acknowledgment

The authors are grateful for the many specific and valuable comments to improve this manuscript.

Nomenclature

C_p = specific heat at constant pressure (J/kg K)
d = diameter of circular cylinder (m)
D = domain
Da = Darcy number (K/L^2)
g = gravitational acceleration (m/s^2)
h = convection heat transfer coefficient (W/(m^2 K)
k = thermal conductivity (W/(m K)
K = permeability of porous medium (m^2)
L = side length of enclosure (m)
n = normal axis
Nu = local Nusselt number
$\overline{\mathrm{Nu}}$ = average Nusselt number
p = pressure (Pa)
P = dimensionless pressure
Pr = Prandtl number
R = radius of cylinder (m)
R_i = residual of weak form
R_k = thermal conductivity ratio
Ra = Rayleigh number, Ra = $\frac{g\beta_f L^3 \Delta T}{\nu_f \alpha_f}$
T = temperature (K)
u = velocity component along x-direction (m/s)
U = dimensional velocity component in x-direction
v = velocity component along y-direction (m/s)
V = dimensional velocity component in y-direction
X_p = thickness of porous layer (m)
x, y = Cartesian coordinates (m)
X, Y = dimensionless Cartesian coordinates

Greek Symbols

α = thermal diffusivity (m^2/s)
β = thermal expansion coefficient (1/K)
$\aleph$ = penalty parameter
δ = angle of inclination
θ = dimensionless temperature
μ = absolute viscosity (Pa·s)
ρ = density (kg/m^3)
υ = kinematic viscosity (m^2/s)
ϕ = nanoparticles volume fraction
φ = shape function
Ψ = stream function
Ω = internal domain

Subscripts

c = cold
f = fluid
h = hot
i, j = residual number
k = node number
n, m = Newton iterative indexes
nf = nanofluid
o = reference point
p = particle
s = solid phase
s = stream

Superscript

h = approximate index

References

[1] Kahwaji, G., and Ali, O. M., 2015, "Numerical Investigation of Natural Convection Heat Transfer From Square Cylinder in an Enclosed Enclosure Filled With Nanofluids," Int. J. Recent Adv. Mech. Eng., **4**(4), pp. 1–17.

[2] Munshi, M. J. H., Bhuiyan, A. H., and Alim, M. A., 2015, "A Numerical Study of Natural Convection in a Square Enclosure With Non-Uniformly Heated Bottom Wall and Square Shape Heated Block," Am. J. Eng. Res. (AJER), **4**(5), pp. 124–137.

[3] De, A. K., and Dalal, A., 2006, "A Numerical Study of Natural Convection Around a Square, Horizontal, Heated Cylinder Placed in an Enclosure," Int. J. Heat Mass Transfer, **49**(23–24), pp. 4608–4623.

[4] Chamkha, A. J., Hussain, S. H., and Abd-Amer, Q. R., 2011, "Mixed Convection Heat Transfer of Air Inside a Square Vented Cavity With a Heated Horizontal Square Cylinder," Numer. Heat Transfer, Part A, **59**(1), pp. 58–79.

[5] Lu, J., Shi, B., Guo, Z., and Chai, Z., 2009, "Numerical Study on Natural Convection in a Square Enclosure Containing a Rectangular Heated Cylinder," Energy Power Eng., **3**(4), pp. 373–380.

[6] Siavashi, M., Bordbar, V., and Rahnama, P., 2017, "Heat Transfer and Entropy Generation Study of Non-Darcy Double-Diffusive Natural Convection in Inclined Porous Enclosures With Different Source Configurations," Appl. Therm. Eng., **110**, pp. 1462–1475.

[7] El Abdallaoui, M., Hasnaoui, M., and Amahmid, A., 2015, "Numerical Simulation of Natural Convection Between a Decentered Triangular Heating Cylinder and a Square Outer Cylinder Filled With a Pure Fluid or a Nanofluid Using the Lattice Boltzmann Method," Powder Technol., **277**, pp. 193–205.

[8] Yu, Z.-T., Fan, L.-W., Hu, Y.-C., and Cen, K.-F., 2010, "Prandtl Number Dependence of Laminar Natural Convection Heat Transfer in a Horizontal Cylindrical Enclosure With an Inner Coaxial Triangular Cylinder," Int. J. Heat Mass Transfer, **53**(7–8), pp. 1333–1340.

[9] Sheikholeslami, M., Gorji-Bandpy, M., and Vajravelu, K., 2015, "Lattice Boltzmann Simulation of Magnetohydrodynamic Natural Convection Heat Transfer of Al_2O_3-Water Nanofluid in a Horizontal Cylindrical Enclosure With an Inner Triangular Cylinder," Int. J. Heat Mass Transfer, **80**, pp. 16–25.

[10] Mehrizi, A. A., Farhadi, M., and Shayamehr, S., 2013, "Natural Convection Flow of Cu-Water Nanofluid in Horizontal Cylindrical Annuli With Inner Triangular Cylinder Using Lattice Boltzmann Method," Int. Commun. Heat Mass Transfer, **44**, pp. 147–156.

[11] Kim, B. S., Lee, D. S., Ha, M. Y., and Yoon, H. S., 2008, "A Numerical Study of Natural Convection in a Square Enclosure With a Circular Cylinder at Different Vertical Locations," Int. J. Heat Mass Transfer, **51**(7–8), pp. 1888–1906.

[12] Yoon, H. S., Ha, M. Y., Kim, B. S., and Yu, D. H., 2009, "Effect of the Position of a Circular Cylinder in a Square Enclosure on Natural Convection at Rayleigh Number of 10^7," Phys. Fluids, **21**(4), p. 047101.

[13] Hussain, S. H., and Hussein, A. K., 2010, "Numerical Investigation of Natural Convection Phenomena in a Uniformly Heated Circular Cylinder Immersed in Square Enclosure Filled With Air at Different Vertical Locations," Int. Commun. Heat Mass Transfer, **37**(8), pp. 1115–1126.

[14] Lee, J. M., Ha, M. Y., and Yoon, H. S., 2010, "Natural Convection in a Square Enclosure With a Circular Cylinder at Different Horizontal and Diagonal Locations," Int. J. Heat Mass Transfer, **53**(25–26), pp. 5905–5919.

[15] Seo, Y. M., Doo, J. H., and Ha, M. Y., 2016, "Three-Dimensional Flow Instability of Natural Convection Induced by Variation in Radius of Inner Circular Cylinder Inside Cubic Enclosure," Int. J. Heat Mass Transfer, **95**, pp. 566–578.

[16] Fu, W.-S., Cheng, C.-S., and Shieh, W.-J., 1994, "Enhancement of Natural Convection Heat Transfer of an Enclosure by a Rotating Circular Cylinder," Int. J. Heat Mass Transfer, **31**(13), pp. 1885–1897.

[17] Roslan, R., Saleh, H., and Hashim, I., 2012, "Effect of Rotating Cylinder on Heat Transfer in a Square Enclosure Filled With Nanofluids," Int. J. Heat Mass Transfer, **55**(23–24), pp. 7247–7256.

[18] Chamkha, A. J., Selimefendigil, F., and Ismael, M. A., 2016, "Mixed Convection in a Partially Layered Porous Cavity With an Inner Rotating Cylinder," Numer. Heat Transfer, Part A, **69**(6), pp. 659–675.

[19] Aly, A. M., Asai, M., and Chamkha, A. J., 2015, "Analysis of Unsteady Mixed Convection in Lid-Driven Cavity Included Circular Cylinders Motion Using an Incompressible Smoothed Particle Hydrodynamics Method," Int. J. Numer. Methods Heat Fluid Flow, **25**(8), pp. 2000–2021.

[20] Gibanov, N. S., Sheremet, M. A., Ismael, M. A., and Chamkha, A. J., 2017, "Mixed Convection in a Ventilated Cavity Filled With a Triangular Porous Layer," Transp. Porous Med., **120**(1), pp. 1–21.

[21] Khozeymehnezhad, H., and Mirbozorgi, S. A., 2012, "Comparison of Natural Convection Around a Circular Cylinder With a Square Cylinder Inside a Square Enclosure," J. Mech. Eng. Autom., **2**(6), pp. 176–183.

[22] Parmananda, M., Khan, S., Dalal, A., and Natarajan, G., 2017, "Critical Assessment of Numerical Algorithms for Convective-Radiative Heat Transfer in Enclosures With Different Geometries," Int. J. Heat Mass Transfer, **108**(Pt. A), pp. 627–644.

[23] Bararnia, H., Soleimani, S., and Ganji, D. D., 2011, "Lattice Boltzmann Simulation of Natural Convection Around a Horizontal Elliptic Cylinder Inside a Square Enclosure," Int. Commun. Heat Mass Transfer, **38**(10), pp. 1436–1442.

[24] Kalyana Raman, S., Arul Prakash, K., and Vengadesan, S., 2012, "Natural Convection From a Heated Elliptic Cylinder With a Different Axis Ratio in a Square Enclosure," Numer. Heat Transfer, Part A, **62**(8), pp. 639–658.

[25] Zhang, P., Zhang, X., Deng, J., and Song, L., 2016, "A Numerical Study of Natural Convection in an Inclined Square Enclosure With an Elliptic Cylinder Using Variational Multiscale Element Free Galerkin Method," Int. J. Heat Mass Transfer, **99**, pp. 721–737.

[26] Roslan, R., Saleh, H., and Hashim, I., 2014, "Natural Convection in a Differentially Heated Square Enclosure With a Solid Polygon," Sci. World J., **2014**, p. 617492.

[27] Tayebi, T., Chamkha, A. J., Djezzar, M., and Bouzerzour, A., 2016, "Natural Convective Nanofluid Flow in an Annular Space Between Confocal Elliptic Cylinders," ASME J. Therm. Sci. Eng. Appl., **9**(1), p. 011010.

[28] Said, B. O., Retiel, N., and Bouguerra, H., 2014, "Numerical Simulation of Natural Convection in a Vertical Conical Cylinder Partially Annular Space," Am. J. Energy Res., **2**(2), pp. 24–29.

[29] Chamkha, A. J., and Ismael, M. A., 2013, "Conjugate Heat Transfer in a Porous Cavity Heated by a Triangular Thick Wall," Numer. Heat Transfer, Part A, **63**(2), pp. 144–158.

[30] Chamkha, A. J., and Ismael, M. A., 2013, "Conjugate Heat Transfer in a Porous Cavity Filled With Nanofluids and Heated by a Triangular Thick Wall," Int. J. Therm. Sci., **67**, pp. 135–151.

[31] Sheremet, M. A., and Trifonova, T. A., 2013, "Unsteady Conjugate Natural Convection in a Vertical Cylinder Partially Filled With a Porous Medium," Numer. Heat Transfer, Part A, **64**(12), pp. 994–1015.

[32] Sheremet, M. A., and Trifonova, T. A., 2014, "Unsteady Conjugate Natural Convection in a Vertical Cylinder Containing a Horizontal Porous Layer: Darcy Model and Brinkman-Extended Darcy Model," Transp. Porous Medium, **101**(3), pp. 437–463.

[33] Basak, T., Roy, S., Paul, T., and Pop, I., 2006, "Natural Convection in a Square Cavity Filled With a Porous Medium Effects of Various Thermal Boundary Conditions," Int. J. Heat Mass Transfer, **49**(7–8), pp. 1430–1441.

[34] Chamkha, A. J., and Ismael, M. A., 2014, "Natural Convection in Differentially Heated Partially Porous Layered Cavities Filled With Nanofluid," Numer. Heat Transfer, Part A, **65**(11), pp. 1089–1113.